Journal of
Materials Chemistry A

Materials for energy and sustainability

Accepted Manuscript

This article can be cited before page numbers have been issued, to do this please use: J. G. Kim, Y. Kim, Y. Kim, D. S. Kim, J. Choi, J. M. Baik and H. K. Yu, *J. Mater. Chem. A*, 2026, DOI: 10.1039/D6TA01732K.

ROYAL SOCIETY OF CHEMISTRY

rsc.li/materials-a

View Article Online
DOI: 10.1039/D6TA01732K

ARTICLE

Synergistic CuO/MgO Nucleation for Low-Supercooling $Na_2SO_4·10H_2O$ in Battery Thermal Management

Received 00th January 20xx,
Accepted 00th January 20xx

DOI: 10.1039/x0xx00000x

Jin Guk Kim [a,b,1], Youngho Kim [b,c], Yeongjin Kim [d,e], Da Seul Kim [d], Jae-Young Choi [d,e,*], Jeong Min Baik [d,*], Hak Ki Yu [a,b,*]

Sodium sulfate decahydrate ($Na_2SO_4·10H_2O$, SSD) is a promising low-temperature phase change material (PCM) but suffers from severe supercooling upon melting. To address this limitation, we developed SSD-based composites incorporating nanostructured flower-like CuO (f-CuO) and porous MgO (p-MgO) as heterogeneous nucleation agents. f-CuO offers high dispersibility, while p-MgO, with a specific surface area approximately 13 times greater than that of f-CuO, exhibits superior spatial overlap with dehydrated SSD clusters. Cooling curve analysis showed that f-CuO and p-MgO individually reduced the supercooling to 5.4 ℃ and 2.7 ℃, respectively. Notably, a hybrid 1:4 mixture (f-CuO:p-MgO) achieved the lowest supercooling of 1.8 ℃. Despite the addition of nucleation agents, the composite maintained a latent heat of 184.8 J g^{-1}, retaining 83 % of pure SSD. Furthermore, when this hybrid SSD composite was coated onto an Al alloy substrate, it delayed the temperature rise by 3.9 ℃ and prolonged the time to reach the target temperature of 50 ℃ by approximately 5 minutes under continuous heating, thereby demonstrating excellent thermal buffering performance. These results highlight the effectiveness of a dual-agent nucleation strategy in minimizing supercooling without compromising heat storage capacity, offering significant potential for passive thermal regulation in lithium-ion battery systems operating in the 30–50 ℃ range.

1. Introduction

Thermal energy storage (TES) has emerged as a critical technology for improving energy efficiency and stability in systems subjected to dynamic thermal environments. Among the various applications, TES plays a particularly vital role in managing temperature fluctuations in advanced electronic and energy systems.[1–3] As one of the most prominent energy storage devices, lithium-ion batteries have seen widespread adoption due to their high energy efficiency and zero local emissions. However, their electrochemical performance is highly temperature sensitive. At elevated temperatures (45-65 ℃), electrolyte decomposition and interfacial reactions can reduce capacity retention to 50-60 % within 50 cycles.[4] At subzero temperatures (~ -10 ℃), lithium plating and increased internal resistance may lead to capacity losses exceeding 20 %.[5] These temperature-dependent degradations threaten battery safety, lifespan, and reliability, underscoring the urgent need for effective thermal regulation.[6] Various active and passive cooling strategies have been proposed, but they often require external control systems or additional energy input. As an alternative, passive TES have attracted increasing attention, particularly in systems subjected to dynamic thermal environments.[7] Among the TES methods, including sensible heat, thermochemical, and latent heat storage, latent heat storage is considered the most effective due to its ability to maintain a nearly constant operating temperature and facilitate rapid heat transfer.[8–14]

In this context, phase change materials (PCMs) based on solid–liquid (S–L) transitions have been widely investigated. Inorganic salt hydrates, particularly sodium sulfate decahydrate ($Na_2SO_4·10H_2O$, SSD), have emerged as promising candidates for low-temperature (melting point of 32.4 ℃) TES systems intended for battery thermal regulation. SSD offers a high latent heat of approximately 254 J g^{-1}, along with non-flammability, non-toxicity, and cost-effectiveness.[15,16] In low-temperature regimes around 30 ℃, SSD and other salt hydrates such as $Na_2CO_3·10H_2O$, $Zn(NO_3)_2·6H_2O$, $FeCl_3·6H_2O$, and $CaCl_2·6H_2O$ have been studied. However, despite these advantages, SSD suffers from intrinsic limitations including severe supercooling, phase separation after dehydration, and low thermal conductivity, which significantly hinder its practical application in battery-integrated TES systems.[16–20] To overcome these challenges, two main approaches have been explored. The first is the use of thickening agents such as carboxymethyl cellulose (CMC), sodium polyacrylate, and polyacrylamide, which help suppress phase separation and promote nucleation. CMC, in particular, has shown effectiveness at concentrations of 3-5 wt%.[21–24] The second strategy involves the incorporation of nucleation agents to induce heterogeneous nucleation. Materials such as Borax, spherical MgO, Cu powder, porous Al_2O_3, Terapod shape ZnO, SiC nanowires, CNT, AlN powder and Expanded Graphite (EG) have been reported to reduce supercooling by lowering nucleation barriers, increasing surface area, and improving thermal

[a] Department of Energy Systems Research, Ajou University, Suwon 16499, South Korea
[b] Department of Materials Science and Engineering, Ajou, University, Suwon 16499, South Korea
[c] Engineering Research Institute, Ajou University, Suwon 16499, Republic of Korea
[d] School of Advanced Materials Science and Engineering, Sungkyunkwan University, Suwon, 16419, Republic of Korea
[e] SKKU of Advanced Institute of Nanotechnology (SAINT), Sungkyunkwan University, Suwon, 16419, Republic of Korea

conductivity.[19,25–38] For a nucleation agent to be effective in salt hydrate PCMs, several key factors should be considered.[22] First, favorable interfacial affinity and chemical compatibility with the PCM are required to facilitate heterogeneous nucleation. Second, a large specific surface area is beneficial for providing abundant nucleation sites. Third, relatively high intrinsic thermal conductivity can assist in improving heat transfer during the phase transition process.

This study aims to effectively suppress the supercooling of SSD and enhance its applicability in battery-integrated TES systems by employing a composite nucleation strategy that combines CuO and MgO in an optimized ratio. This hybrid approach simultaneously improves dispersion compatibility and thermal conductivity, offering a synergistic effect that has been rarely addressed in previous TES-related studies. CuO and MgO were selected based on their earth abundance, low cost, and superior thermal conductivities (3-19 W $m^{-1}K^{-1}$ for CuO and 48 W $m^{-1}K^{-1}$ for MgO), which are significantly higher than that of SSD (0.554 W $m^{-1}K^{-1}$).[19,39,40] CuO was synthesized in a nanoflower structure to enhance aqueous dispersibility and surface area. In contrast, MgO synthesized in our previous study in a porous nanoflower form exhibited over ten times the surface area of CuO, but showed lower dispersibility.[41] Given that porous architectures have been reported to enhance interactions with water molecules, which may facilitate hydration-related nucleation at the MgO/SSD interface.[42] Interestingly, MgO exhibited dispersion behavior similar to SSD, suggesting compatibility in heterogeneous nucleation despite its lower absolute dispersibility. Based on this, SSD composites were fabricated using flower-like CuO (f-CuO), porous MgO (p-MgO), and a 1:4 mixture of the two as nucleation agents, along with CMC as a thickening agent. Cooling curve analysis showed that supercooling was suppressed to 5.4 ℃ with f-CuO, 2.7 ℃ with p-MgO, and 1.8 ℃ with the hybrid composition. In addition, DSC analysis confirmed that the SSD composite (SSD-C) exhibited a latent heat of 184.8 J g^{-1}, corresponding to approximately 83 % of the value measured for pure SSD (222.9 J g^{-1}). Furthermore, application of the SSD-C to aluminum alloy substrates demonstrated a significantly reduced heating rate under external thermal input, confirming its thermal buffering effect and applicability as a practical TES material for battery thermal management.

2. Experimental

2.1 Materials

Copper(II) nitrate trihydrate ($Cu(NO_3)_2·3H_2O$, 99 %), urea ($CO(NH_2)_2$, 98 %), ethylene glycol ($C2H6O2$, 99 %), sodium sulfate decahydrate ($Na_2SO_4·10H_2O$, 98 %), carboxymethylcellulose sodium (CMC), magnesium chloride hexahydrate ($MgCl_2·6H_2O$, 98 %), sodium carbonate anhydrous (Na_2CO_3, 99.5 %), and sodium hydroxide (NaOH, 97 %) were all purchased from Daejung Chemical & Materials Co., Ltd. (Korea). Thermal grease (MX-4 thermal compound) was supplied by Arctic.

2.2 Synthesis of flower-like CuO

Flower-like CuO (f-CuO) was synthesized via a hydrothermal method, as illustrated in Fig. 1. In a typical procedure, 3 g of $Cu(NO_3)_2·3H_2O$ and 7.5 g of urea were dissolved in a mixed solvent of 40 mL deionized (DI) water and 10 mL ethylene glycol (EG) under stirring for 30 min. The resulting precursor solution was transferred into a 100 mL Teflon-lined stainless steel autoclave, which was then sealed and heated at 100 ℃ for 6 h in a box oven. After cooling the autoclave rapidly under running water, the as-synthesized product was collected by centrifugation at 8000 rpm for 10 min and washed three times with DI water to remove residual ions. The final product was dried overnight to obtain the f-CuO powder.

2.3 Synthesis of porous MgO

Porous MgO (p-MgO) was synthesized via a hydrothermal method. First, 4.24 g of Na_2CO_3 and 0.4 g of NaOH were dissolved in 80 mL of deionized (DI) water under stirring. Subsequently, 80 mL of 0.5 M aqueous $MgCl_2·6H_2O$ solution was added, and the resulting 160 mL mixed solution was stirred for 10 min. The final white suspension was transferred to a 200 mL Teflon-lined stainless steel autoclave, sealed completely, and subjected to hydrothermal treatment at 160 ℃ for 1 h in a box furnace with a heating rate of 1 ℃ min^{-1}. Upon completion, the autoclave was rapidly cooled. The resulting product was washed thoroughly with DI water and dried overnight at 80 ℃ to obtain the porous MgO powder.

2.4 Synthesis of Sodium sulfate decahydrate composite

Sodium sulfate decahydrate ($Na_2SO_4·10H_2O$, SSD), nucleation agents, and a thickening agent were combined to a total weight of 20 g and sealed in a glass vial. The mixture was melted in a water bath at 60 ℃ for 30 min to fully dissolve the components. For all SSD-C, carboxymethyl cellulose (CMC, 3 wt%, 0.6 g) was used as the thickening agent. For SSD-C(f-CuO), f-CuO was employed as the

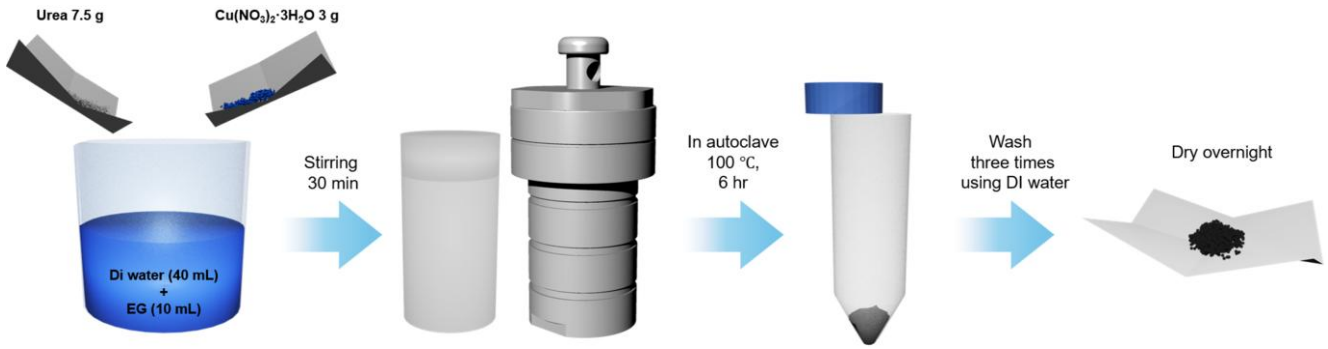

Fig. 1 Schematic of the Synthesis method of flower-like CuO.

View Article Online
DOI: 10.1039/D5TA01733K

nucleation agent at varying contents of 1-5 wt% (0.2-1.0 g). For SSD-C(p-MgO), p-MgO was added at varying contents of 1-5 wt% (0.2-1.0 g) under the same preparation conditions. To prepare the hybrid SSD-C samples, the total amount of nucleation agents was fixed at 2.5 wt% (0.5 g), and f-CuO and p-MgO were added at different mass ratios of 3:2, 2:3, 1:4, and 1:8. For the optimized SSD-C(1:4) sample, f-CuO and p-MgO were added at 0.5 wt% (0.1 g) and 2.0 wt% (0.4 g), respectively. After the addition of the nucleation agents, each mixture was sealed and stirred for 1 h to obtain a homogeneous SSD composite.

2.5 Materials characterization

The crystal structure of the powder samples was analyzed by X-ray diffraction (XRD, Rigaku Ultima III) using Cu Kα radiation (λ= 0.154 nm). The morphology and exposed crystal facets of the particles were examined using scanning electron microscopy (JEOL, JSM-6700F) and transmission electron microscopy (JEOL/CEOS, JEM-2100F equipped with a Cs corrector). Nitrogen adsorption desorption isotherms were recorded on a Micromeritics ASAP 2020 Plus to determine the specific surface area, pore size distribution, and total pore volume. The thermal energy storage performance of the composites was evaluated using differential scanning calorimetry (NETZSCH, DSC 200 F3 Maia).

2.6 Measurement of Supercooling Performance

The molten SSD-C, prepared by stirring in a 60 ℃ water bath, was transferred into a sealed cylindrical vial to prevent water evaporation. The vial was then placed inside a thermally insulated enclosure maintained at 10 ℃ to minimize external heat exchange. A K-type thermocouple with a resolution of 0.01 ℃ was inserted into the sample to record the temperature as a function of time during the cooling process.

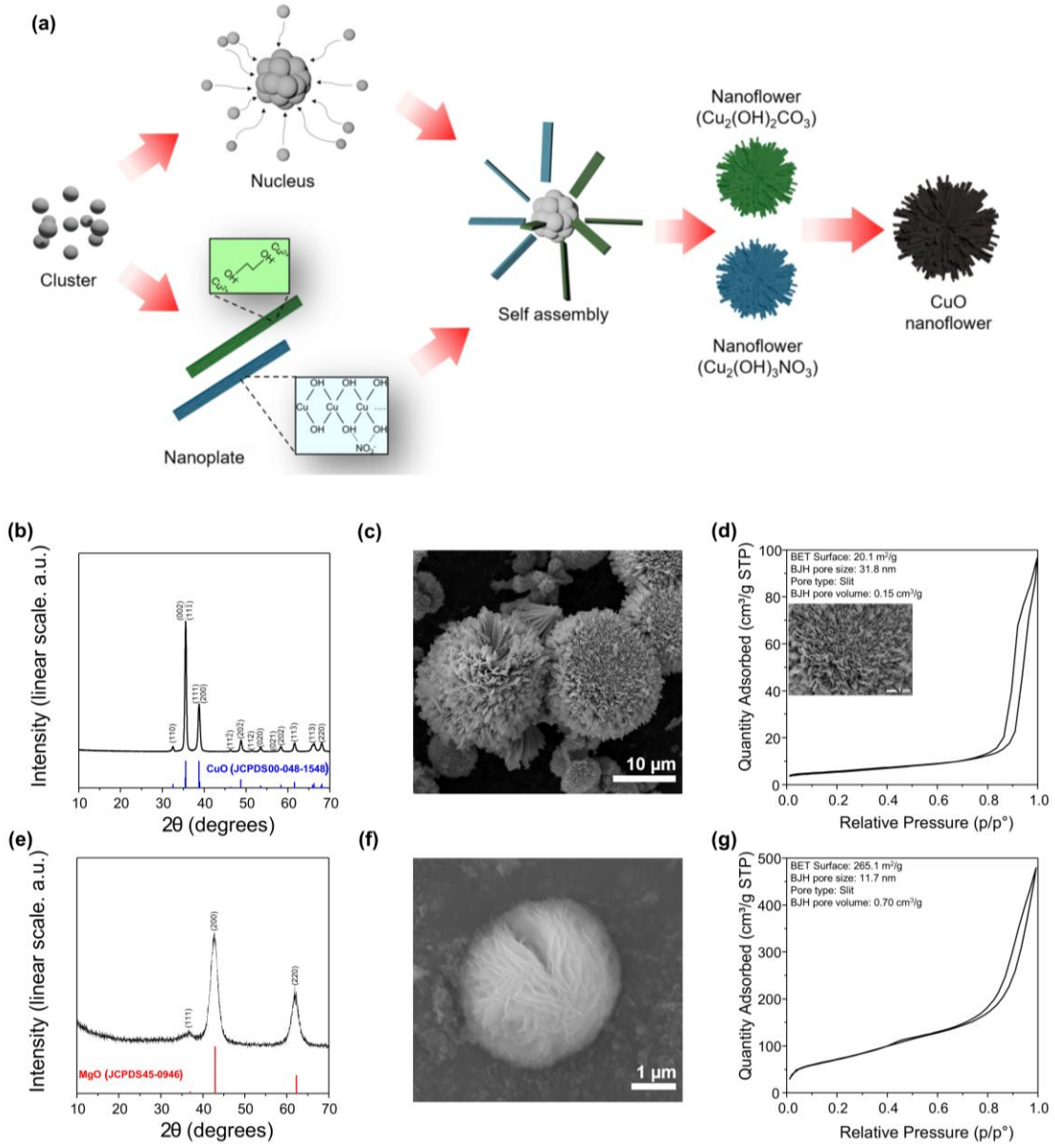

Fig. 2 (a) Schematic of Formation Mechanism of flower-like CuO via Self-Assembly and Calcination, (b) XRD pattern of f-CuO, (c) SEM image of f-CuO, (d) Nitrogen adsorption/desorption isotherms of f-CuO, (e) XRD pattern of p-MgO, (f) SEM image of p-MgO, and (g) Nitrogen adsorption/desorption isotherms of p-MgO.

View Article Online
DOI: 10.1039/D6TA01730K

2.7 Measurement of Thermal Buffering Performance

An aluminium-based alloy disk (diameter 50 mm, height 10 mm, 56.74 g), tightly laminated with aluminum foil, was placed on a hot plate maintained at 60 °C. The surface temperature of the disk was monitored using an infrared (IR) camera (FLUKE, TiS20+ MAX THERMAL IMAGER) at 60 s intervals over the range of 30–50 °C. The same procedure was applied to the Al-ad coated with SSD-C(1:4). For both samples, a sufficient amount of thermal grease was applied between the disk and the hot plate to ensure efficient thermal contact.

To minimize the effect of the low infrared emissivity of the Al-alloy surface, a high-emissivity carbon tape was attached to the side surface of the disk. The emissivity of the IR camera was set to 0.95 based on the carbon tape region, and the temperature was recorded from this calibrated region.[43]

3. Results and Discussion

3.1 Mechanism of flower-like CuO

Fig. 2(a) is a schematic diagram illustrating the synthesis mechanism of f-CuO, which proceeds via two distinct pathways. The first pathway, corresponding to Equations (1)–(3), begins with the formation of CuO seeds as primary clusters aggregate into nuclei. During this step, urea decomposes in aqueous solution, releasing NH_4^+ and concurrently generating CO_2 and OH^-. The CO_2 subsequently reacts with water to form H_2CO_3, which is then converted into CO_3^{2-}.[44] Meanwhile, ethylene glycol (EG), a polymeric chain terminated with hydroxyl groups, coordinates with Cu^{2+} ions, thereby directing the anisotropic growth of CuO.[45] The resulting coordination complex reacts with CO_3^{2-} and OH^- ions derived from urea, forming $Cu_2(OH)_2CO_3$ (Fig. S1).[46] These nanoplates undergo successive radial self-assembly around the initial nucleus, gradually evolving into a nanoflower-like architecture (Fig. S2). Upon calcination at 500 °C, the $Cu_2(OH)_2CO_3$ nanoflowers undergo a phase transformation to f-CuO.

$$5Cu(NO_3)_2 + 8CO(NH_2)_2 + 9(CH_2OH)_2 + 22H_2O \rightarrow 5Cu^{2+} + 10NO_3^- + 26NH_4HCO_3 \quad (1)$$

$$2Cu^{2+} + 2NH_4HCO_3 \rightarrow Cu_2(OH)_2CO_3 + 2NO_2 + 4H_2O \quad (2)$$

$$Cu_2(OH)_2CO_3 \rightarrow 2CuO + CO_2 + H_2O \quad (3)$$

The second pathway, following Equations (4)–(7), involves a similar initial nucleation step. In this case, $Cu(NO_3)_2$ dissociates in aqueous solution to yield Cu^{2+} and NO_3^-. The OH- ions released from urea react with Cu^{2+} to form tetrahedral $[Cu(OH)_4]^{2-}$, which subsequently precipitates as $Cu(OH)_2$. The NO_3^- ions are stabilized via hydrogen bonding with the hydroxyl groups of $[Cu(OH)_4]^{2-}$, leading to the formation of $Cu_2(OH)_3NO_3$ (Fig. S1).[47–49] This precursor grows into nanoplates that radially assemble around the nucleus, resulting in a nanoflower morphology (Fig. S2). A final calcination step at 500 °C converts this intermediate into f-CuO.

$$Cu(NO_3)_2 + CO(NH_2)_2 + (CH_2OH)_2 + 2H_2O \rightarrow Cu^{2+} + 2NO_3^- + 4OH^- \quad (4)$$

$$Cu^{2+} + 4OH^- \rightarrow [Cu(OH)_4]^{2-} \quad (5)$$

$$[Cu(OH)_4]^{2-} + Cu(OH)_2 + NO_3^- \rightarrow Cu_2(OH)_3NO_3 + 3OH^- \quad (6)$$

$$2Cu_2(OH)_3NO_3 \rightarrow 4CuO + 2NO_2 + O_2 + 3H_2O \quad (7)$$

These results demonstrate that the characteristic radial nanoflower morphology of CuO originates from two distinct precursor-mediated growth pathways, each governed by unique coordination interactions and phase transformation mechanisms.

3.2 Characterization of Nucleation agents

Fig. 2(b) and (e) present the X-ray diffraction (XRD) patterns of f-CuO and p-MgO, respectively. In f-CuO (Fig. 2(b)), distinct diffraction peaks appear at 2θ values of 32.4°, 35.5°, 38.7°, 46.24°, 48.7°, 51.32°, 53.46°, 58.3°, 61.6°, 65.84°, 66.24°, and 68.04°, which correspond to the monoclinic CuO phase (a = 4.6883 Å, b = 3.4229 Å, c = 5.1319 Å, β = 99.506°) according to JCPDS Card No. 00-048-1548. In Fig. 2(e), p-MgO shows sharp diffraction peaks at 36.58°, 42.66°, and 61.84°, matching JCPDS Card No. 45-0946 and confirming a cubic rock salt MgO phase (a = b = c = 4.2112 Å, α = β = γ = 90°). The slight peak broadening observed for p-MgO can be attributed to nanoscale crystallite domains and local structural heterogeneity associated with its porous architecture, rather than to reduced crystallinity. Fig. 2(c) and (f) display secondary electron microscopy (SEM) images of f-CuO and p-MgO, respectively. f-CuO in Fig. 2(c) exhibits a spherical architecture composed of radially arranged nanoplates converging toward the center, with an overall diameter of approximately 15 μm. This nanoflower morphology offers a large surface area, and in this study, each nanoplate is considered to act as a heterogeneous nucleation site for SSD, promoting effective nucleation. Furthermore, the uniform and adequately spaced nanoplate growth contributes to improved spatial uniformity in heterogeneous nucleation. The p-MgO in Fig. 2(f) presents a porous spherical morphology with numerous macropores, and the particle diameter is measured to be approximately 3.55 μm.

Fig. 2(d), (g) show the nitrogen adsorption–desorption isotherms and Barrett–Joyner–Halenda (BJH) pore distribution curves of f-CuO and p-MgO, respectively, providing quantitative analysis of the morphological features observed in SEM. For f-CuO in Fig. 2(d), the Brunauer–Emmett–Teller (BET) surface area is 20.1 m^2/g, and the average pore size obtained from BJH analysis is 31.8 nm, indicating a mesoporous structure. The isotherm exhibits a clear hysteresis loop, corresponding to a type IV isotherm with an H3 hysteresis according to the IUPAC classification, which is typical of slit-like pores with non-rigid, plate-like structures—consistent with the nanoplate assembly observed in Fig. 2(c). The relatively low pore volume further suggests the presence of wide-mouthed, shallow slit-shaped pores, formed by tightly packed nanoplates around the center. This morphology may facilitate heterogeneous nucleation of SSD by providing accessible surface area and sufficient spatial volume for initial nucleus formation and stabilization. In Fig. 2(g), p-MgO demonstrates a BET surface area of 265.1 m^2/g—approximately 13 times higher than that of f-CuO and an average pore diameter of

View Article Online
DOI: 10.1039/D5TA01732K

11.7 nm, also within the mesoporous range. It likewise exhibits a type IV isotherm with H3 hysteresis, consistent with the slit-like pores formed between the "petals" observed in Fig. 2(f). Comprehensive analysis of the BJH data indicates that p-MgO possesses a pore morphology characterized by narrow entrances and wider internal cavities, forming an intricate porous network. This structure contributes to enhanced surface area and mass transport, which can be advantageous for promoting diffusion and providing additional nucleation sites for SSD.

3.3 Supercooling Performance of SSD composite

Initially, f-CuO was introduced as the nucleation agent, and the degree of supercooling suppression was evaluated under varying concentrations to determine the optimal content. Subsequently, f-CuO was replaced with p-MgO under the same conditions to compare their relative nucleation performances. Finally, an SSD-C containing a mixture of f-CuO and p-MgO was fabricated to investigate the synergistic effect on supercooling suppression via cooling curve analysis.

Fig. 3(a) shows the cooling curves of SSD-C with f-CuO (SSD-C(f-CuO)) added at various weight percentages (0–5 wt%), and Fig. 3(b) summarizes the corresponding supercooling degrees. In the case of pure SSD, the phase transition began at 16.3 °C. As the temperature reached 20.3 °C, partial latent heat release was observed, accompanied by a temperature decrease. This indicates that nucleation occurred far below the theoretical phase change temperature of SSD (32.4 °C), and the full phase transition did not proceed. This phenomenon is attributed to ineffective homogeneous nucleation, despite partial phase separation being suppressed by the presence of CMC. When f-CuO was added in the range of 1–5 wt% (Fig. S3), the phase change onset temperature increased gradually up to 2.5 wt%, indicating enhanced heterogeneous nucleation and suppressed supercooling. However, beyond this point, particularly at 5 wt%, the

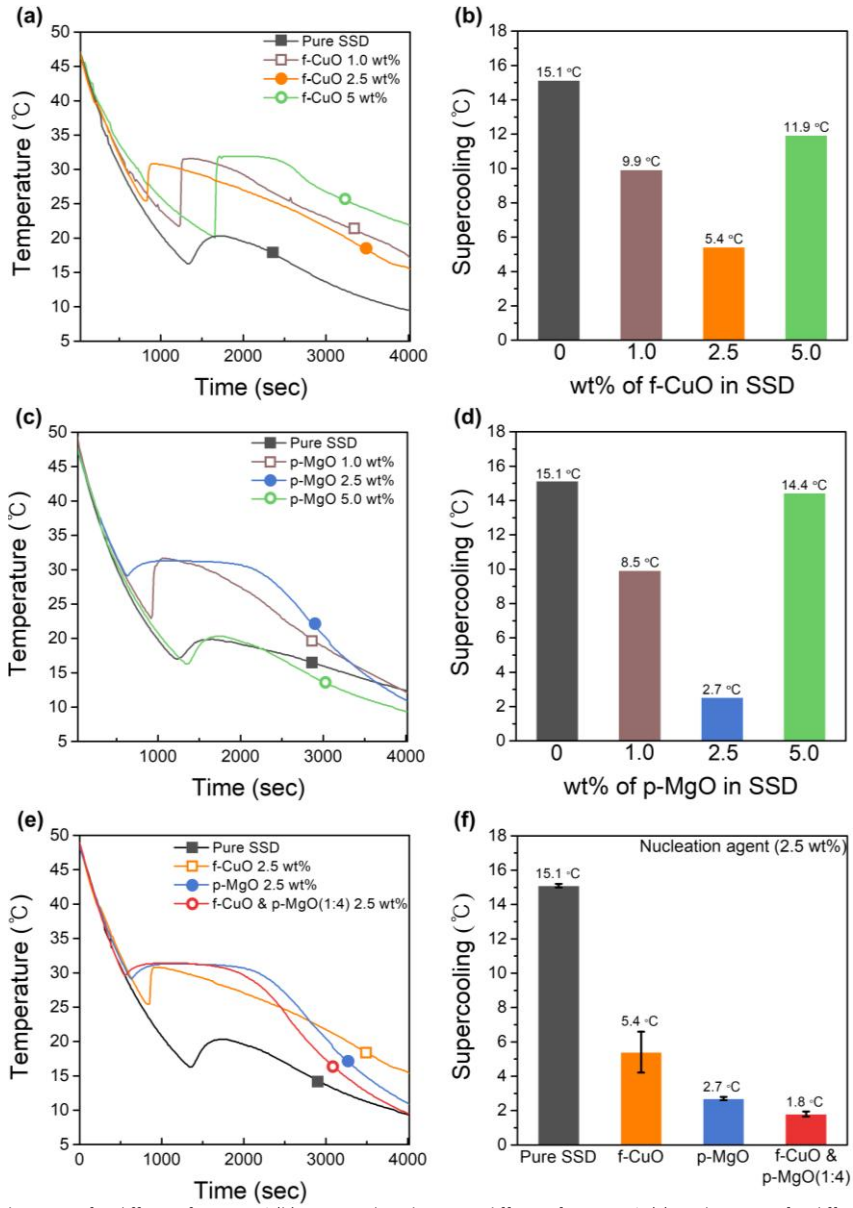

Fig. 3 Cooling curve data. (a) Cooling curve for different f-CuO wt% (b) Supercooling degree at different f-CuO wt%, (c) Cooling curve for different p-MgO wt%, (d) Supercooling degree at different p-MgO wt%, (e) Cooling curves for different nucleation agent (2.5 wt%), and (f) Supercooling degree at different nucleation agents (2.5 wt%).

View Article Online DOI: 10.1039/D5TA01772K

degree of supercooling increased again. As shown in the quantitative data in Fig. 3(b), the minimum supercooling (5.4 ℃) occurred at 2.5 wt% f-CuO, whereas the value increased to 11.9 ℃ at 5 wt%. This suggests that while f-CuO acts as an effective nucleation agent, excessive loading (5 wt%) induces particle agglomeration and subsequent sedimentation, which severely disrupts dispersion homogeneity. Such sedimentation lowers the availability of active nucleation sites within the bulk, ultimately hindering heterogeneous nucleation. These findings confirm that 2.5 wt% f-CuO represents the optimal concentration to promote efficient nucleation and suppress supercooling in SSD-C.

Similarly, Fig. 3(c) shows the cooling curves of SSD-C with p-MgO added at various weight percentages (0-5 wt%), and Fig. 3(d) summarizes the corresponding supercooling degrees. When p-MgO was added in the range of 1-5 wt%, the phase change onset temperature increased gradually, indicating enhanced heterogeneous nucleation and suppressed supercooling. As shown in the quantitative data in Fig. 3(d), the minimum supercooling degree of 2.7 ℃ was obtained at 2.5 wt% p-MgO, where the phase transition initiated at 29.0 ℃ and reached a maximum temperature of 31.4 ℃ during the phase change. However, further increasing the p-MgO content to 5 wt% increased the supercooling degree and induced partial phase separation, likely because excessive p-MgO loading caused particle aggregation and sedimentation. Notably, the minimum supercooling degree achieved with 2.5 wt% p-MgO was markedly lower than that obtained with 2.5 wt% f-CuO, indicating the higher nucleation efficiency of p-MgO under the same loading condition.

Finally, the effect of the relative composition of f-CuO and p-MgO was further examined under a fixed total nucleation-agent loading of 2.5 wt%. When f-CuO and p-MgO were combined at mass ratios of 3:2 and 2:3, SSD-C exhibited partial phase transitions, with the phase transition terminating at 20.3 ℃ and 20.7 ℃, respectively, as shown in Fig. S4. In contrast, SSD-C(1:4) showed a complete phase transition and the lowest supercooling degree of 1.8 ℃, as confirmed by the comparative cooling curves and quantitative supercooling values in Fig. 3(e) and (f). However, further increasing the p-MgO fraction to 1:8 increased the supercooling degree to 9.7 ℃, as also shown in Fig. S4. These results indicate that optimized supercooling suppression is achieved not by simply increasing the p-MgO fraction, but by balancing the relative contributions of f-CuO and p-MgO in the hybrid nucleation system. The error bars in Fig. 3(f) represent the standard deviation obtained from repeated cooling-curve measurements, and the corresponding values are summarized in Table S1.

Moreover, after reaching the peak temperature of 31.4 ℃, the cooling rate of SSD-C(1:4) was faster than that of SSD-C with p-MgO alone, but slower than that of SSD-C with f-CuO alone. This behavior reflects differences in thermal conductivity across the SSD matrix. In the case of SSD-C(f-CuO), f-CuO is uniformly dispersed throughout the material, which enhances bulk thermal conductivity and results in a more rapid temperature decrease following phase change. Conversely, in SSD-C(p-MgO), p-MgO particles exhibit less uniform dispersion, leading to lower overall thermal conductivity. Although phase change initiates earlier in SSD-C(p-MgO) than in SSD-C(f-CuO), the transition proceeds more slowly, and the subsequent cooling rate is also reduced.

In the SSD-C(1:4) system, the two nucleating agents exhibit improved overall dispersion. The fine-scale dispersion of f-CuO is complemented by the moderate aggregation behavior of p-MgO, resulting in enhanced spatial overlap between SSD clusters and nucleation sites. As a result, heterogeneous nucleation is more readily triggered, and the thermal conductivity surpasses that of SSD-C(p-MgO), leading to a comparable holding time at peak temperature but a noticeably faster cooling rate. These combined effects suggest that SSD-C(1:4) exhibits superior heat release characteristics and may serve as a more effective thermal energy storage medium for low-temperature battery thermal management systems (LT-BTMS) in lithium-ion batteries.

3.4 Mechanism of SSD-C nucleation

The supercooling phenomenon of SSD arises from the insufficient free energy driving force for homogeneous nucleation at the melting point, which leads to a large ΔG^{homo} and significantly reduces the nucleation rate. According to classical nucleation theory, the nucleation rate is governed by Equation (8), where the dominant term is $\exp(-\Delta G^*/k_BT)$ indicating that the magnitude of ΔG^* has a critical influence on nucleation behavior. Reducing ΔG^* is therefore a key strategy to accelerate nucleation, and the nucleation agent employed in this study effectively lowers ΔG^* under heterogeneous nucleation conditions.

$$\boldsymbol{I^{st}} = \boldsymbol{N_o}\exp\left(\frac{-\Delta G^*}{k_BT}\right)\cdot \boldsymbol{k^+}(\boldsymbol{n^*})\cdot \boldsymbol{z} \quad (8)$$

($\boldsymbol{I^{st}}$: Steady-state nucleation rate, ΔG^*: The critical work for heterogeneous nucleation, $\boldsymbol{N_o}$: Number of heterogeneous nucleation site, $\boldsymbol{k^+}(\boldsymbol{n^*})$: Attachment rates, z: Zeldovich factor, $\boldsymbol{k_B}$: Boltzmann constant)

$$\Delta \boldsymbol{G^{het}} = \{\boldsymbol{V}\cdot\Delta \boldsymbol{g} + \boldsymbol{S}\cdot\boldsymbol{\sigma_{\alpha\beta}}\}\cdot \boldsymbol{f}(\boldsymbol{\theta}) = \Delta \boldsymbol{G^{homo}}\cdot \boldsymbol{f}(\boldsymbol{\theta}) \quad (9)$$

(V: Volume of nucleus, S: Surface of nucleus, f(θ): catalytic factor, ΔG^{het}: Work for heterogeneous nucleation, ΔG^{homo}: Work for homogeneous nucleation)

$$\boldsymbol{f}(\boldsymbol{\theta}) = \frac{2-3cos\theta+cos^3\theta}{4}$$ ($\boldsymbol{\theta}$: Contact angle) (10)

In heterogeneous nucleation, ΔG^* is expressed as ΔG^{homo} multiplied by the catalytic factor f(θ), which is defined in Equation (9). This factor f(θ) depends on the wetting angle θ and generally lies within the range $0 \le f(\theta) \le 1$. As θ decreases, f(θ) also decreases, resulting in a reduced ΔG^* and thereby facilitating nucleation. In the present system, SSD forms nuclei in the form of spherical caps on an H_2O layer adsorbed to the surface of the solid nucleation agent. This configuration establishes a defined wetting angle and satisfies the condition $\Delta G^{hetero} < \Delta G^{homo}$.[50]

Transmission electron microscopy (TEM) analysis (Fig. 4(a)–(c)) revealed that f-CuO adopts a nanoplate architecture with predominant exposure of the (110) facet. This surface is terminated with O^{2-} ions, forming an O-terminated structure characterized by high surface energy and a strongly negative charge. [51,52] When exposed to water,

H_2O molecules dissociate into H^+ and OH^- species. The H^+ ions are chemisorbed onto surface O^{2-} sites, while OH^- species coordinate with surface Cu^{2+} ions, forming Cu–OH bonds. These surface hydroxyl groups attract Na^+ ions from the solution, and subsequently, SO_4^{2-} anions are electrostatically adsorbed onto the positively polarized regions of the Cu–OH sites. This sequential adsorption process facilitates the formation of primary Na_2SO_4 nuclei. The ion-mediated nucleation pathway on the O-terminated CuO (110) surface is summarized in Fig. 4(i)-(1). Upon interaction with surrounding water molecules, these primary nuclei evolve into $Na_2SO_4 \cdot nH_2O$ hydrate seeds, which serve as templates for further nucleation and growth of SSD clusters. In addition, the adsorbed hydroxyl layer on f-CuO induces a secondary H_2O layer via hydrogen bonding, which acts as a hydrophilic interface for additional Na_2SO_4 cluster attachment and SSD nucleation. These two pathways collectively reduce the solid–liquid interfacial energy and establish a favorable contact angle (θ), thereby significantly decreasing the nucleation barrier (ΔG*).

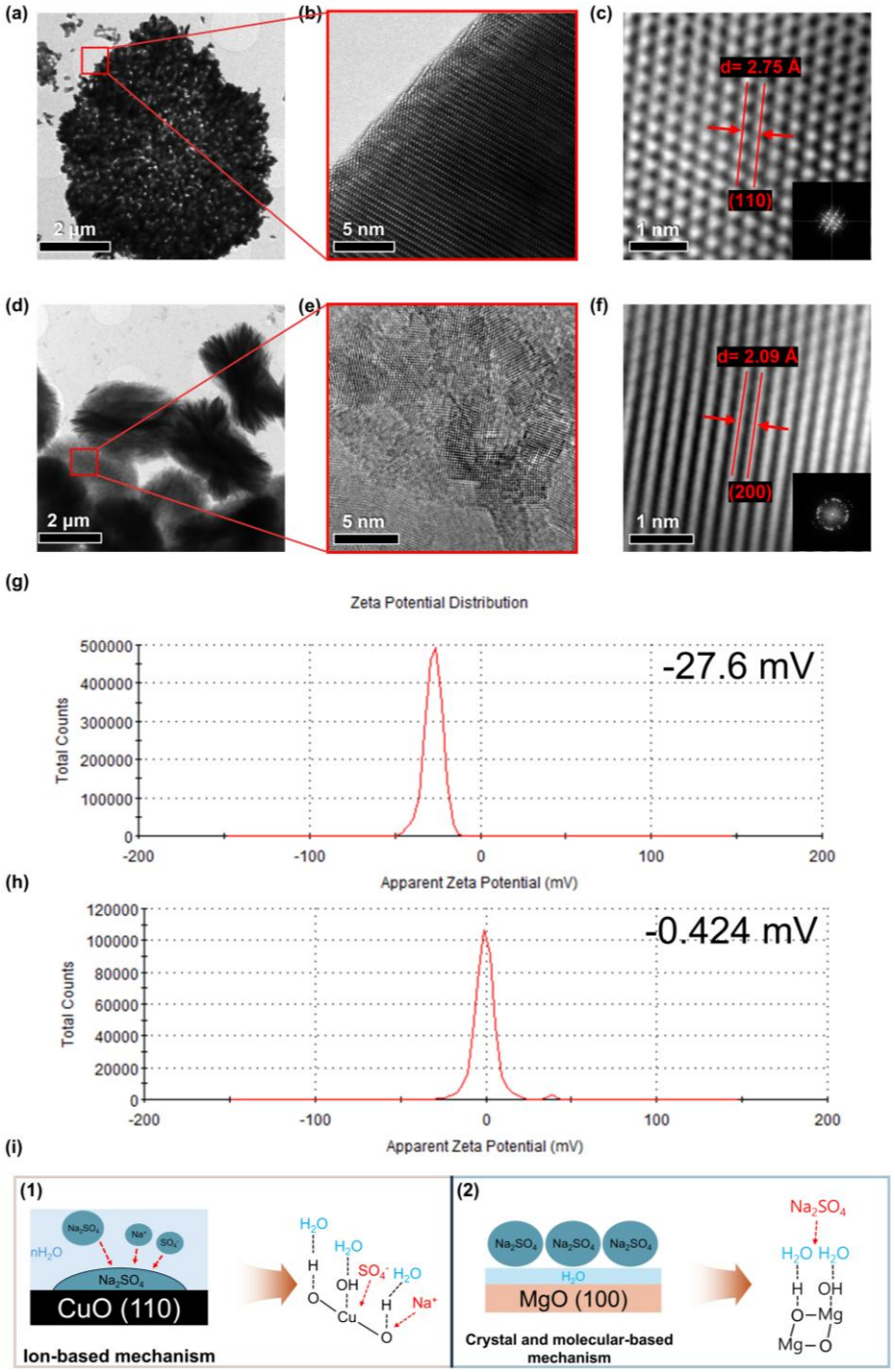

Fig. 4 (a) Low resolution of TEM image of f-CuO, (b) High magnification TEM image of the red-boxed area in (a), (c) Fourier-filtered image of single f-CuO inset: corresponding Fourier-transformed diffraction pattern, (d) low resolution of TEM image of p-MgO, (e) High magnification TEM image of the red-boxed area in (d), (f) Fourier-filtered image of single p-MgO Inset: corresponding Fourier-transformed diffraction pattern, (g) Zeta potential analysis of f-CuO in water, (h) Zeta potential analysis of p-MgO in water and (i) Comparison of ion based and crystal/molecular-based heterogeneous nucleation mechanism on CuO (110) and MgO (100).

View Article Online DOI: 10.1039/D5TA04277B

Furthermore, zeta potential measurements (Fig. 4 (g)) show that f-CuO possesses a strongly negative surface charge of -27.6 mV, consistent with the O-terminated (110) surface observed in Fig. 4(c). Despite this stable dispersion (Fig. S6(a)), the strong negative charge may induce electrostatic repulsion with negatively charged Na_2SO_4 clusters, especially those stabilized by CMC. Although this repulsion may not directly alter the contact angle, it could hinder the approach and adsorption stability of SSD clusters on the f-CuO surface, thereby potentially limiting nucleation efficiency.

According to TEM analysis (Fig. 4(d)-(f)), p-MgO exhibits a stable rock salt structure with terrace planes grown along the (200) facet and an almost neutral surface charge. Although this facet has inherently low surface energy, the polarization of surrounding H_2O molecules in aqueous solution induces dissociation into H^+ and OH^-. OH^- is chemisorbed onto Mg^{2+} sites, while H^+ is chemisorbed onto O^{2-}, forming surface Mg–OH and OH^- groups. These surface species facilitate the formation of a stable hydration layer through hydrogen bonding. [53] In addition, p-MgO may undergo partial surface hydration under the mildly alkaline SSD environment, forming hydroxylated Mg-containing surface species rather than undergoing complete transformation into $Mg(OH)_2$.[54] This possible surface hydration can further stabilize interfacial water molecules and supports the hydration-assisted heterogeneous nucleation pathway proposed in this study.

Zeta potential measurements (Fig. 4(h)) show that p-MgO exhibits a very low surface potential of -0.424 mV, indicating poor dispersion behavior (Fig. S6(b)), which originates from the weak negative surface charge associated with the surface OH^- layer. While the SSD nucleation mechanism on p-MgO resembles that of f-CuO, the absence of strong surface charge limits nucleation via electrostatic adsorption of ionic species such as Na^+ and SO_4^{2-}. Instead, nucleation proceeds predominantly through physisorption of Na_2SO_4 clusters onto the hydrogen-bonded H_2O layer. This crystal and molecular-based nucleation pathway on the MgO (100) surface is schematically illustrated in Fig. 4(i)-(2). The hydration layer provides a sufficiently stable and energetically favorable interface for nucleation. These surface characteristics directly influence the structure and stability of the hydration layer, which governs the interfacial energy between the SSD nucleus and the substrate. As a result, both f-CuO and p-MgO effectively lower ΔG^*, promote SSD nucleation, and suppress supercooling.

In addition to ΔG^* reduction, increases in the number density of critical nuclei (N_o) and the attachment rate ($k^+(n^*)$) also enhance the overall nucleation rate [50]. These parameters correspond to the pre-exponential factor in Equation (8), and when ΔG^* is fixed, they determine the frequency and speed of actual nucleation events. In this study, we identified that an increased specific surface area of the nucleation agent, as well as dispersion consistency with Na_2SO_4 clusters formed after SSD dehydration, are key factors contributing to the enhancement of both N_o and k^+. First, the specific surface area of the nucleation agent, which provides available nucleation sites, is a key factor that can increase both N_o and k^+. As shown in Fig. 2(f) and 2(g), p-MgO possesses a specific surface area approximately 13 times greater than that of f-CuO, thereby offering a significantly larger number of nucleation sites. As a result, both N_o and k^+ are expected to be higher for p-MgO, making it a more effective nucleation agent. Second, when the degree of dispersion between the nucleation agent and precursor clusters is similar, both phases are spatially distributed within overlapping regions of the solution, which maximizes the likelihood of their mutual contact. As this spatial overlap increases, the actual frequency of nucleation events also increases, leading to a higher N_o. Furthermore, k^+, defined as the probability of a precursor successfully reaching and attaching to a nucleus surface, is also enhanced. Thus, dispersion compatibility plays a critical role in determining the nucleation rate.

The zeta potential measurements further support the dispersion contrast between the two nucleation agents. f-CuO exhibits a strongly negative surface potential of -27.6 mV, indicating stable dispersion, whereas p-MgO shows a near-neutral value of −0.424 mV and tends to aggregate more readily. The Na_2SO_4 clusters display similarly poor dispersibility (Fig. S6(d)), to the extent that their zeta potential could not be reliably measured. In contrast, the combined system exhibited an intermediate zeta potential of -5.42 mV (Fig. S6(e)), indicating partial electrostatic stabilization by f-CuO. These results suggest that the combined system retains partial aggregation while gaining limited electrostatic stabilization, supporting the proposed coexistence of relatively dispersed f-CuO-rich regions and p-MgO-associated clustered regions.

Fig. 5(a) presents a conceptual schematic and corresponding cluster population profile illustrating the height-dependent dispersion behavior of f-CuO and p-MgO at a 1:4 ratio in molten SSD. Based on the zeta potential results discussed earlier, p-MgO exhibits limited dispersion stability and tends to accumulate in the lower region of the vial. This region corresponds to the cluster-dominant zone, where poorly dispersed Na_2SO_4 clusters are primarily located. Within this zone, p-MgO functions as the principal nucleation agent, facilitating nucleation and subsequent crystal growth.

In contrast, f-CuO maintains uniform dispersion throughout the molten phase. While it can serve as a supplementary nucleation site within the cluster-dominant region, its contribution becomes more significant in the upper ion-accessible region, where the density of pre-formed Na_2SO_4 clusters is relatively low and free Na^+ and SO_4^{2-} species remain available for nucleation. In this region, f-CuO enhances nucleation probability through an ion-based mechanism by promoting ionic adsorption and interfacial enrichment of Na^+ and SO_4^{2-} near the surface. This surface-induced ionic accumulation increases the effective local driving force for nucleation without altering the bulk composition of the molten SSD.

As a result, the heterogeneous dispersion characteristics enable spatially differentiated nucleation pathways. p-MgO provides a high local nucleation probability within the cluster-dominant region owing to its large specific surface area and dispersion behavior comparable to that of Na_2SO_4 clusters, whereas f-CuO extends nucleation opportunities in the ion-accessible region via its ion-mediated mechanism. The complementary interaction between these two nucleation agents ultimately leads to more effective nucleation when applied simultaneously than when either age nt is used independently.

View Article Online
DOI: 10.1039/D6TA01773K

Fig. 5(b) and (c) show SEM images and elemental mapping of SSD nucleated and grown on f-CuO and p-MgO, respectively. In Fig. 5(b), SSD crystals filled the gaps between the nanoplates of spherical CuO nanoflowers, as confirmed in more detail in Fig. S5. Elemental mapping shows Cu confined to the spherical region, while Na, S, and O are distributed over a wider area. The overlay image confirms that the nanoplates of f-CuO provided heterogeneous nucleation sites, contributing to a large effective surface area. In Fig. 5(c), SSD grown covered the surface of spherical p-MgO. Elemental mapping shows Mg localized within the spherical region, whereas Na, S, and O are more broadly distributed. The overlay image demonstrates that the

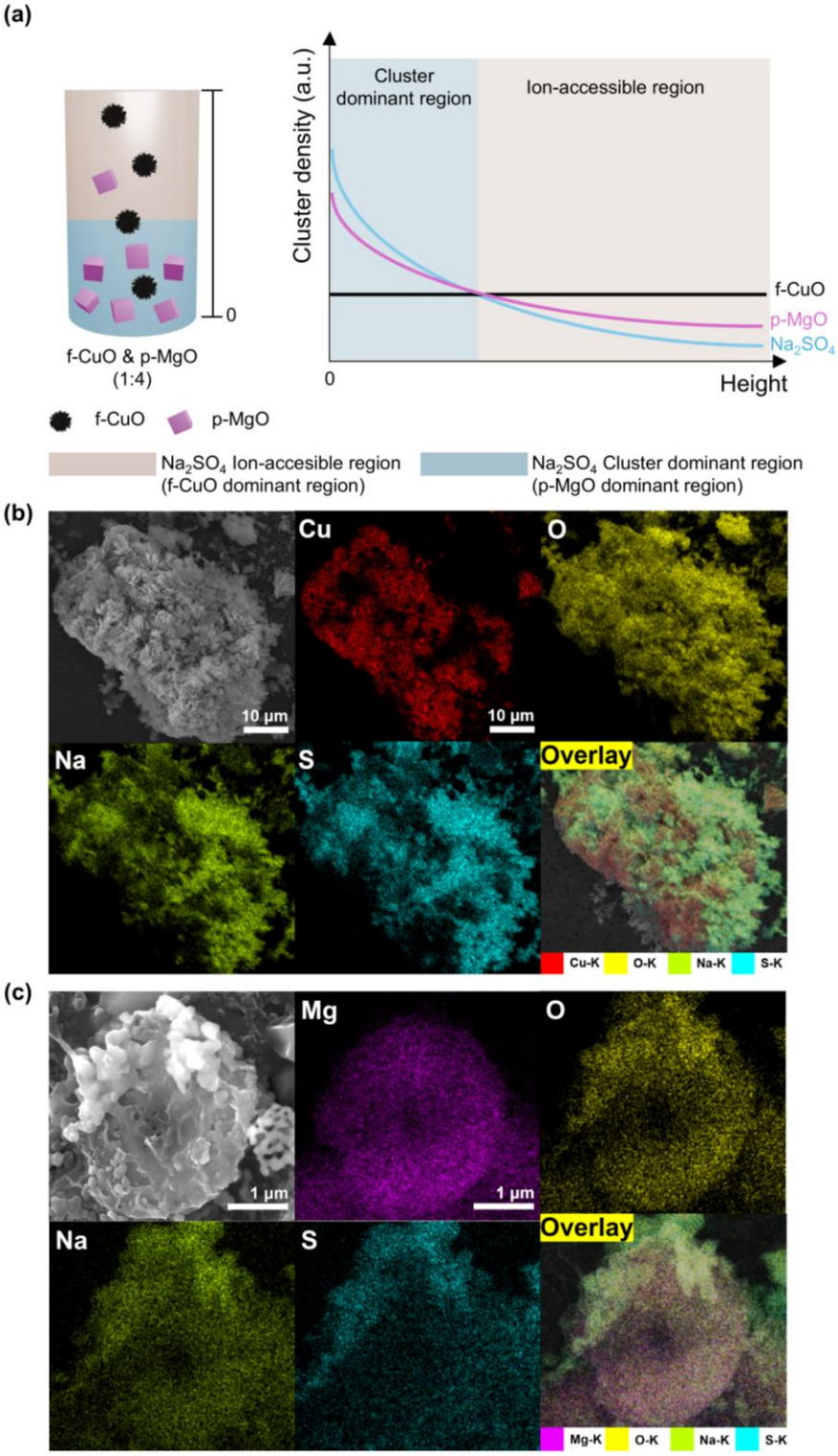

Fig. 5 (a) Schematic illustration and corresponding height-dependent cluster profile of f-CuO and p-MgO (1:4) distribution in molten SSD, (b) SEM image of SSD grown on CuO, Cu, O, Na, S elemental mapping images, and overlay of all elemental mapping images. (c) SEM image of SSD grown on MgO, Mg, O, Na, S elemental mapping images, and overlay of all elemental mapping images.

porous structure and large surface area of p-MgO effectively promoted heterogeneous nucleation of SSD.

3.5 Heat storage performance

Fig. 6 shows the results of evaluating the heat storage performance by applying f-CuO, p-MgO, and their mixture as nucleation agents. The corresponding latent heat enthalpy (ΔH) values are summarized in Table 1. The phase change onset temperature of pure SSD was 34 ℃, and ΔH was 222.9 J g^{-1}, indicating the highest heat storage capacity among the tested conditions.

For the f-CuO series, ΔH gradually decreased with an increasing addition ratio, as shown in Fig. S7 and Table S2. This trend is interpreted as the result of heterogeneous nucleation being promoted and supercooling being effectively suppressed; however, the f-CuO may also act as an impurity, inducing a metastable state and thereby reducing the total latent heat. When f-CuO was used as the nucleation agent, the SSD-C condition with 2.5 wt% addition showed the most effective supercooling control. Its phase change onset temperature was 33.3 ℃, and the latent heat (ΔH) was 175.6 J g^{-1}, which is about 79 % of that of pure SSD.

In contrast, when 2.5 wt% p-MgO was applied at the same concentration, SSD-C exhibited a phase change onset temperature of 33.9 ℃ and a ΔH of 206.5 J g^{-1}, indicating superior heat storage performance compared to 2.5 wt% f-CuO. The p-MgO results in Fig. S7 and Table S2 further support that this condition maintained a high latent heat with stable crystallization behavior. This improvement is believed to result from the enhanced stability of recombination between Na_2SO_4 and H_2O molecules, leading to the formation of $Na_2SO_4 \cdot nH_2O$ with a higher hydration number (n). Additionally, the high specific surface area of p-MgO likely facilitated further bonding with H_2O molecules.

Table 1 Comparison of Latent Heat for Different Nucleation Agents.

Sample	Latent heat (ΔH) [Jg^{-1}]
Pure SSD	-222.9
SSD + f-CuO 2.5 wt%	-175.6
SSD + p-MgO 2.5 wt%	-206.5
SSD + f-CuO & p-MgO(1:4) 2.5 wt%	-184.8

In the case of SSD-C prepared by mixing f-CuO and p-MgO at a 1:4 ratio, the phase change onset temperature was 33.8 ℃ and ΔH was 184.8 J g^{-1}, achieving 83 % of the heat storage density compared to pure SSD. This condition exhibited better heat storage performance than f-CuO alone but was still lower than that of p-MgO alone. These results suggest that, under mixed conditions, p-MgO served as the primary nucleation agent, while f-CuO played a secondary role by offering widespread nucleation sites. In particular, the reduced total amount of p-MgO compared to its single use appears to be the main reason for the decrease in ΔH in the mixed condition.

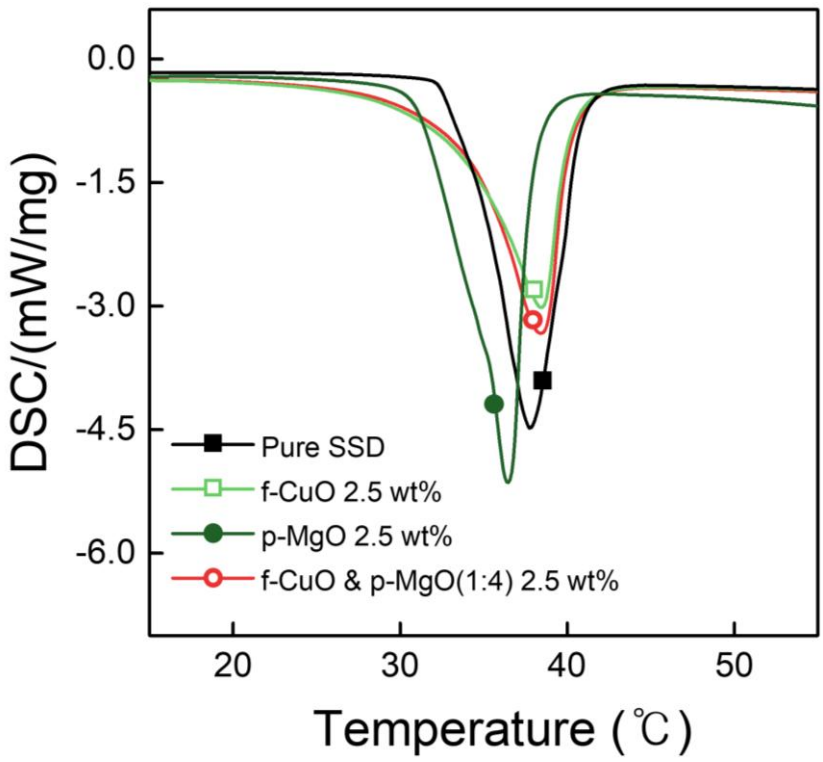

Fig. 6 DSC curves of pure SSD and SSD composites containing f-CuO (2.5 wt%), p-MgO (2.5 wt%), and a hybrid formulation (f-CuO & p-MgO(1:4) 2.5 wt%).

To further clarify the significance of the heat storage performance, the supercooling degree and latent heat of the present SSD-C(1:4) system were compared with previously reported SSD-based composites, as summarized in Table S3. Several reported SSD-based systems employ borax as a primary nucleation agent. Secondary additives such as graphite, graphene nanoplatelets, or Al/C nanoparticles are often introduced to improve heat transfer or structural stability within the PCM matrix. In contrast, the present f-CuO/p-MgO system uses nucleation agents with relatively high intrinsic thermal conductivities. Therefore, these agents can contribute to both heterogeneous nucleation and thermal transport without requiring additional thermally conductive fillers. Despite achieving a very low supercooling degree of 1.8 ℃, SSD-C(1:4) retained a latent heat of 184.8 J g^{-1}. This value is comparable to or higher than those of several previously reported SSD-based systems. These results indicate that the dual-agent nucleation strategy effectively balances supercooling suppression and latent heat retention.

3.6 Temperature Rise Buffering Effect of SSD-C

The coating configuration of SSD-C(1:4) applied onto an Al alloy disk (Al-ad, 19.6 cm^3) is schematically illustrated in Fig. 7(a). An 8 g layer of SSD-C(1:4) was coated on the Al-ad surface to evaluate its thermal buffering performance. The temperature increase behavior of the coated and uncoated specimens was measured using an IR camera to simulate the thermal control application potential of aluminum in lithium-ion battery (LIB) packaging materials. The temperature change was observed until the specimen surface reached approximately 50 °C while the hot plate was maintained at 60 °C. Fig. 7(b) shows the surface temperature change of pure Al-ad without SSD-C, and Fig. 7(c) shows the temperature distribution of Al-ad coated with SSD-C(1:4). Pure Al-ad started at approximately 30 ℃ and reached 49.9 ℃ after 960 sec, whereas the specimen coated with SSD-C(1:4) rose to 46.0 ℃ under the same conditions, showing a temperature that was approximately 3.9 ℃ lower and a relatively slower temperature increase rate.

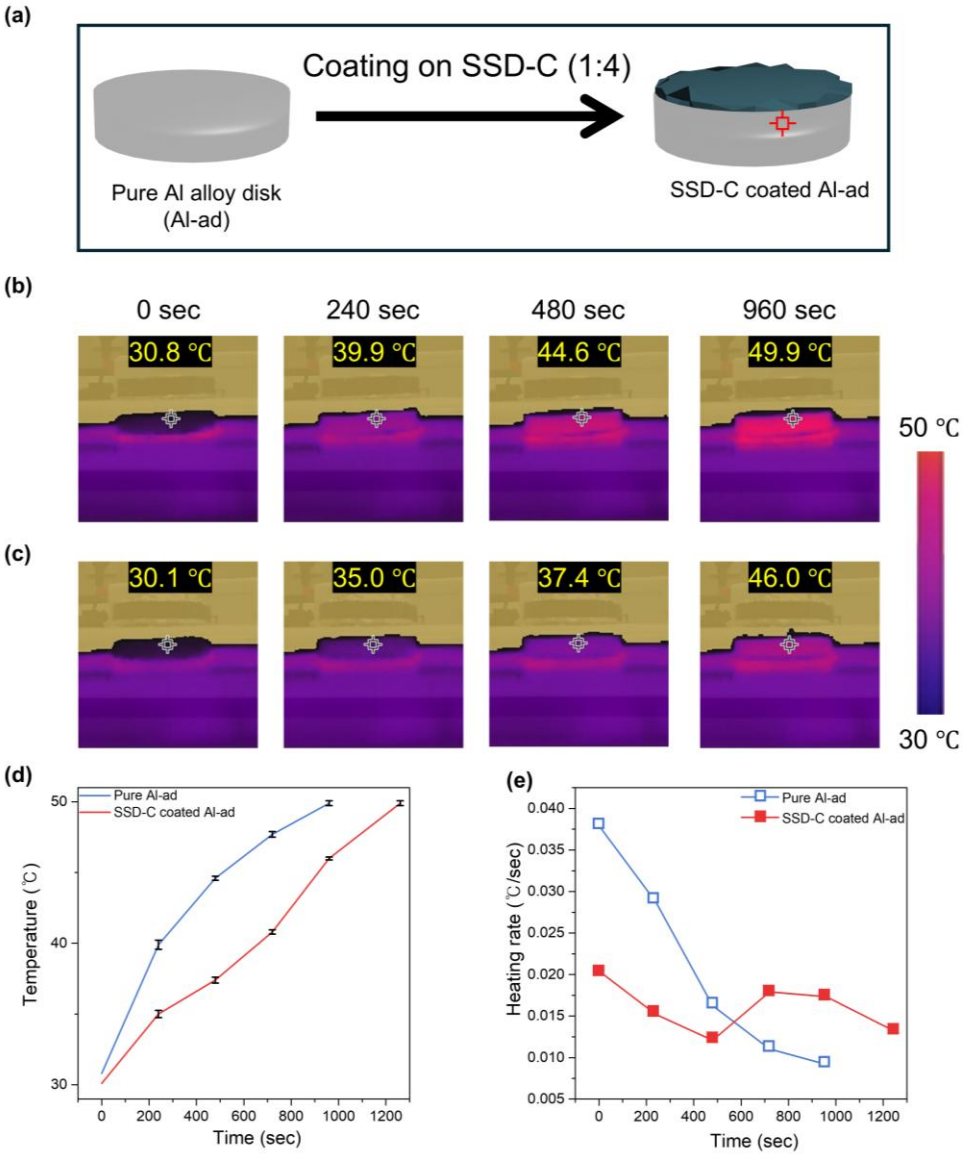

Fig. 7 (a) Schematic of SSD-C (1:4) coating on Al-ad, (b) Infrared image of Pure Al alloy, (c) Infrared image of SSD-C(1:4) coated Al-ad, (d) Time-dependent temperature of Al-ad with and without SSD-C coating and (e) Time-dependent heating rate of Al-ad with and without SSD-C coating.

To better understand this difference, the temperature change over time was analyzed to evaluate the thermal behavior of the samples, as shown in Fig. 7(d). Error bars were added to Fig. 7(d) based on repeated measurements, and the corresponding temperature standard deviation values are summarized in Tables S4 and S5. In the case of pure Al-ad, a steep temperature increase occurs at the beginning, followed by a gradual saturation curve as it approaches the temperature of the hot plate. This indicates a characteristic of gradual saturation without any inflection point. Fig. 7(e) is a graph showing the heating rate (℃ sec^{-1}), obtained by differentiating the temperature data of Fig. 7(d) with respect to time. Pure Al-ad exhibits an overall decreasing trend, forming a monotonically decreasing curve without any extreme value. On the other hand, for the Al-ad coated with SSD-C, a clear inflection point appears around 480 s and 720 s in both Fig. 7(d) and (e), and in particular, an extreme value appears at these points in the heating rate graph. In the initial 0–200 sec section, the heating rate of the SSD-C(1:4) coated Al-ad was 0.0204 ℃ sec^{-1}, which is only about 53 % of the 0.0379 ℃ sec^{-1} observed for pure Al-ad. This is interpreted as a result of delayed temperature rise due to latent heat absorption around 32 ℃, the melting point of SSD-C(1:4). In addition, in the 400–720 sec section, the heating rate reached its lowest point at 480 sec, at which the phase change of SSD-C(1:4) was completed, and then temporarily increased before decreasing again. This suggests that, after the latent heat absorption had ended, the heat storage effect of SSD-C(1:4) disappeared, and the specimen gradually moved toward thermal equilibrium as it approached the temperature of the hot plate.

As a result, it was confirmed that the SSD-C(1:4) coating effectively reduced the heating rate of Al-ad, thereby delaying the temperature rise within the optimal operating temperature range of LIBs, which lies between 30 and 40 ℃. Specifically, the 8 g coating applied to the 19.63 cm^3 Al-ad delayed the temperature rise by 300 sec, corresponding to 15.3 sec cm^{-3} of Al-ad and 37.5 sec per gram of SSD-C. This suggests that SSD-C-based coating materials can be effectively applied to LIB thermal management.

Conclusions

In this study, we proposed a composite nucleation agent to effectively suppress the intrinsic supercooling of $Na_2SO_4 \cdot 10H_2O$ (SSD), a hydrate-based phase change material, while maintaining its thermal storage performance. Flower-like CuO nanostructures (f-CuO) and porous MgO (p-MgO) were synthesized and applied to SSD individually or in a 1:4 mixed ratio to systematically evaluate nucleation efficiency and thermal properties. Cooling curve analysis revealed that 2.5 wt% f-CuO resulted in a supercooling degree of 5.4 ℃, while p-MgO at the same concentration reduced it to 2.7 ℃. Notably, the f-CuO & p-MgO(1:4) composite achieved the most effective supercooling suppression of 1.8 ℃. This enhancement is attributed to the similarity in dispersion behavior between p-MgO and the SSD dehydration products, its large specific surface area (265.1 $m^2 g^{-1}$), and the uniform distribution of f-CuO, which facilitates spatially uniform nucleation throughout the matrix. DSC analysis confirmed that the optimized SSD composite (SSD-C) maintained approximately 83 % of the latent heat capacity of pure SSD (184.8 J g^{-1}), demonstrating reliable thermal energy storage. Furthermore, thermal buffering performance was validated by coating SSD-C(1:4) on an aluminum alloy disk. Within the critical temperature range of 30–50 ℃, SSD-C(1:4) delayed the peak surface temperature rise by approximately 3.9 ℃ and exhibited a pronounced delay in the 35–40 ℃ interval. These results demonstrate that the SSD-C can simultaneously achieve low-temperature phase change storage and thermal regulation, making it a promising candidate for passive thermal energy storage (TES) systems in lithium-ion batteries. The findings suggest that composite nucleation strategies can contribute to improving the thermal stability of practical energy storage systems and provide a platform for future high-performance TES material development.

Author contributions

J. G. K conducted the overall experiments and synthesis and wrote the manuscript. Y. Kim supported the synthesis of porous MgO. Y. J. K assisted with the zeta potential measurements. D. S. K supported the IR camera measurements. J.-Y. C, J. M. B and H. K. Y supervised the whole project.

Conflicts of interest

There are no conflicts to declare.

Data availability

The data that support the findings of this study are contained within the Supplementary Information (SI) accompanying this article.

Acknowledgements

This work was supported by the National Research Foundation of Korea(NRF) grant funded by the Korea government (MSIT) (No. RS-2023-00208311).

Notes and references

1 R. Bidiyasar, R. Kumar and N. Jakhar, *Energy Storage*, 2024, **6**, e639.
2 R. K. Rajamony, J. K. S. Paw, A. K. Pandey, A. G. N. Sofiah, A. Yadav, Y. C. Tak, T. S. Kiong, A. Mohanty, M. E. M. Soudagar and Y. Fouad, *Energy Storage*, 2024, **6**, e679.
3 I. Dincer, *Int. J. Energy Res.*, 2002, **26**, 567–588.
4 T. M. Bandhauer, S. Garimella and T. F. Fuller, *J. Electrochem. Soc.*, 2011, **158**, R1.
5 X. Wu, W. Wang and J. Du, *Int J Energy Res*, 2020, **44**, 1775–1788.
6 Y. Abdul-Quadir, T. Laurila, J. Karppinen, K. Jalkanen, K. Vuorilehto, L. Skogström and M. Paulasto-Kröckel, *Int. J. Energy Res.*, 2014, **38**, 1424–1437.
7 S. Landini, J. Leworthy and T. S. O'Donovan, *Journal of Energy Storage*, 2019, **25**, 100887.
8 I. Sarbu and A. Dorca, *Int J Energy Res*, 2019, **43**, 29–64.
9 J. Aarts, H. Fischer, O. Adan and H. Huinink, *Journal of Energy Storage*, 2025, **114**, 115726.
10 N. Zhang, Y. Yuan, X. Cao, Y. Du, Z. Zhang and Y. Gui, *Adv Eng Mater*, 2018, **20**, 1700753.
11 S. Ben Romdhane, A. Amamou, R. Ben Khalifa, N. M. Saïd, Z. Younsi and A. Jemni, *Journal of Building Engineering*, 2020, **32**, 101563.
12 I. Sarbu and C. Sebarchievici, *Sustainability*, 2018, **10**, 191.
13 S. N. Avghad, A. J. Keche and A. Kousal, *Thermal Energy Storage*, 2016, **13**, 72–77.
14 L. Zhang, X. Xia, Y. Lv, F. Wang, C. Cheng, S. Shen, L. Yang, H. Dong, J. Zhao and Y. Song, *Journal of Energy Storage*, 2023, **72**, 108279.
15 J. Hirschey, K. R. Gluesenkamp, A. Mallow and S. Graham, 2018, **3653**, 1–9.
16 B. K. Purohit and V. S. Sistla, *Energy Storage*, DOI:10.1002/est2.212.
17 L. Gao, X. Zhang and W. Hua, *Journal of Energy Storage*, 2024, **84**, 110723.
18 H. Cui, W. Zhang, H. Yang, Y. Zou, J. Liu and J. Yan, *Energy*, 2024, **303**, 132010.
19 J. Hirschey, M. Goswami, D. O. Akamo, N. Kumar, Y. Li, T. J. LaClair, K. R. Gluesenkamp and S. Graham, *Journal of Energy Storage*, 2022, **52**, 104949.
20 C. He, H. Chen, Z. Huang, Z. Song, X. Liu, S. Gao, J. Zhang, X. Zhang, Y. Jiang and H. Gao, *Journal of Energy Storage*, 2025, **128**, 117245.
21 G. Feng, X. Xu, N. He, H. Li and K. Huang, *Materials Research Innovations*, 2015, **19**, S5-972-S5-977.
22 M. Goswami, N. Kumar, Y. Li, J. Hirschey, T. J. LaClair, D. O. Akamo, S. Sultan, O. Rios, K. R. Gluesenkamp and S. Graham, *Journal of Applied Physics*, DOI:10.1063/5.0049512.
23 P. Hou, J. Mao, F. Chen, Y. Li and X. Dong, 2018, **11**, 2230.
24 R. S. Abdul Hamza and M. A. Habeeb, *Trans. Electr. Electron. Mater.*, 2024, **25**, 77–88.
25 Y. Wang, K. Yu, H. Peng and X. Ling, *Energy*, 2019, **167**, 269–274.
26 P. Sundaram, A. Sathishkumar, R. Prabakaran, P. G. Kumar and S. C. Kim, *Journal of Energy Storage*, 2023, **72**, 108257.
27 X.-Y. Zhang, L.-N. Wang, S.-Z. Li, N. Jiang, Y.-Y. Song, J. Yang, Z. Wei and W. Yang, *Journal of Energy Storage*, 2025, **116**, 116076.
28 T. Wang, W. Cui, X. Li, T. Ma and Q. Wang, *Journal of Energy Storage*, 2024, **85**, 111083.
29 W. Cui, Y. Yuan, L. Sun, X. Cao and X. Yang, *Renewable Energy*, 2016, **99**, 1029–1037.
30 L. Que and X. Zhang, *Journal of Energy Storage*, 2022, **54**, 105360.
31 J. Thakkar, S. B. Annavajjala, J. Kosny and M. J. Sobkowicz, *Journal of Energy Storage*, 2024, **91**, 111936.
32 P. Manoj Kumar, M. S. Karuna, M. S. Sureshkumar, M. Lal Rinawa, R. Sakthivel, K. Muthukumar and E. Kathir Malavan, *Materials Today: Proceedings*, DOI:10.1016/j.matpr.2023.02.297.
33 X. Zhang, Z. Tan, L. Geng, J. Zhao and C. Liu, *Journal of Energy Storage*, 2024, **99**, 113345.
34 K. Huang, T. Mi, C. Zheng, L. Wang and X. Yi, *Journal of Energy Storage*, 2024, **89**, 111734.
35 W. Chen, Q. Chen, Y. Yu, H. Gao and B. Ma, *ChemPlusChem*, DOI:10.1002/cplu.202400542.
36 W. Sun, G. Liang, F. Feng, H. He and Z. Gao, *Journal of Energy Storage*, 2022, **55**, 105857.
37 P. Hu, D.-J. Lu, X.-Y. Fan, X. Zhou and Z.-S. Chen, *Solar Energy Materials and Solar Cells*, 2011, **95**, 2645–2649.
38 W. Wu, S. Lu, Q. Lin, Z. Wu, L. Yao and B. Shi, *Journal of Energy Storage*, 2025, **114**, 115756.
39 J. Sathish Kumar, G. Senthilkumar and S. Ramachandran, *Case Studies in Thermal Engineering*, 2023, **52**, 103723.
40 S. R. Nfawa, A. R. Abu Talib, A. A. Basri and S. U. Masuri, *Case Studies in Thermal Engineering*, 2021, **27**, 101279.
41 Y. Kim, X. Dong, S. Chae, G. Asghar, S. Choi, B. J. Kim, J. Choi and H. K. Yu, *Advanced Materials*, 2023, **35**, 2204775.
42 S. Kalingani, S. N. Das, S. Bhuyan and L. Sahoo, *Trans. Electr. Electron. Mater.*, 2024, **25**, 636–652.
43 M. C. Larciprete, S. Paoloni, N. Orazi, F. Mercuri, M. Orth, Y. Gloy, M. Centini, R. Li Voti and C. Sibilia, *International Journal of Thermal Sciences*, 2019, **146**, 106109.
44 M. A. Dar, Q. Ahsanulhaq, Y. S. Kim, J. M. Sohn, W. B. Kim and H. S. Shin, *Applied Surface Science*, 2009, **255**, 6279–6284.
45 J. Liu, J. Jin, Z. Deng, S.-Z. Huang, Z.-Y. Hu, L. Wang, C. Wang, L.-H. Chen, Y. Li, G. Van Tendeloo and B.-L. Su, *Journal of Colloid and Interface Science*, 2012, **384**, 1–9.
46 M. Zhou, Y. Gao, B. Wang, Z. Rozynek and J. O. Fossum, *Eur J Inorg Chem*, 2010, **2010**, 729–734.
47 B. Liu, *Nanoscale*, 2012, **4**, 7194.
48 N. Ba, L. Zhu, H. Li, G. Zhang, J. Li and J. Sun, *Solid State Sciences*, 2016, **53**, 23–29.
49 M. Outokesh, M. Hosseinpour, S. J. Ahmadi, T. Mousavand, S. Sadjadi and W. Soltanian, *Ind. Eng. Chem. Res.*, 2011, **50**, 3540–3554.
50 K. Kelton and A. L. Greer, *Nucleation in Condensed Matter - Applications in Materials and Biology*, Elsevier, 2010, vol. 15.
51 J. L. V. Moreno, A. A. B. Padama and H. Kasai, *CrystEngComm*, 2014, **16**, 2260.
52 W. Xiang, J. Liu, M. Chang and C. Zheng, *Chemical Engineering Journal*, 2012, **200–202**, 91–96.
53 K. Jug, B. Heidberg and T. Bredow, *J. Phys. Chem. C*, 2007, **111**, 6846–6851.
54 O. Fruhwirth, G. W. Herzog, I. Hollerer and A. Rachetti, *Surface Technology*, 1985, **24**, 301–317.

View Article Online
DOI: 10.1039/D6TA01732K

Data availability

The data that supports the findings of this study are available from the corresponding author, upon reasonable request.